

# Rapid Quadrotor Navigation in Diverse Environments using an Onboard Depth Camera

Jonathan Lee, Abhishek Rathod, Kshitij Goel, John Stecklein, and Wennie Tabib



(a) Cave

(b) Industrial tunnel

(c) Forest

Fig. 1: (a) Tight spaces, (b) high amounts of particulate matter such as dust and (c) thin obstacles such as branches are hazards found in search and rescue environments. To aid search teams, autonomous aerial systems must rapidly navigate these dangers without posing additional risks for rescuers or victims. This paper proposes a rapid quadrotor navigation system, which uses forward-arc motion primitives and a forward-facing depth camera to achieve speeds up to 6 m/s in cluttered environments. Safety is achieved by executing a safe stopping action when no feasible action is found. Experiments are conducted in diverse environments, including caves and forests. A video of these experiments may be found at <https://youtu.be/tk8vUot0gD4>

**Abstract**—Search and rescue environments exhibit challenging 3D geometry (e.g., confined spaces, rubble, and breakdown), which necessitates agile and maneuverable aerial robotic systems. Because these systems are size, weight, and power (SWaP) constrained, rapid navigation is essential for maximizing environment coverage. Onboard autonomy must be robust to prevent collisions, which may endanger rescuers and victims. Prior works have developed high-speed navigation solutions for autonomous aerial systems, but few have considered safety for search and rescue applications. These works have also not demonstrated their approaches in diverse environments. We bridge this gap in the state of the art by developing a reactive planner using forward-arc motion primitives, which leverages a history of RGB-D observations to safely maneuver in close proximity to obstacles. At every planning round, a safe stopping action is scheduled, which is executed if no feasible motion plan is found at the next planning round. The approach is evaluated in thousands of simulations and deployed in diverse environments, including caves and forests. The results demonstrate a 24% increase in success rate compared to state-of-the-art approaches.

maneuverable, but are limited by battery capacity and flight time. Therefore, these systems must rapidly navigate through the environment. More importantly, onboard autonomous navigation must be robust as collisions endanger rescuers and victims. To achieve these goals in highly cluttered environments with narrow gaps, it is advantageous to leverage smaller size robots equipped with a lightweight, short-range depth camera as opposed to a heavy, long-range LiDAR.

In this work, a rapid quadrotor navigation methodology is proposed, which leverages a forward-facing, limited field-of-view RGB-D camera to operate in diverse environments (e.g., caves, sewers, forests, industrial tunnels) without scene-specific parameter tuning or training. A reactive planner is developed using forward-arc motion primitives, which are differentiable up to jerk and continuous up to snap to enable aggressive flight. Motion primitive selection is based on a perception front-end that searches a history of RGB-D observations to safely maneuver in close proximity to obstacles.

The contributions of this work are: (1) a reactive navigation framework that uses a history of depth observations to evaluate a library of forward-arc motion primitives; (2) a trajectory scheduling approach to prevent collisions; (3) extensive photo-realistic simulations with 3150 trials in diverse cluttered environments; and (4) hardware experiments covering 571 m in successful trials without collisions and achieving a maximum speed of 6 m/s. The results demonstrate a 24% higher success rate compared to state-of-the-art approaches.

## I. INTRODUCTION

Extreme search and rescue environments exhibit challenging 3D geometry (e.g., confined spaces, rubble, breakdown), which preclude rapid traversal by legged, wheeled, and tracked robotic systems. Quadrotors are highly agile and

\*This work was supported in part by the U.S. Army Research Office and the U.S. Army Futures Command under Contract No. W519TC-23-C-0031. The authors are with the Robotics Institute, Carnegie Mellon University, Pittsburgh, PA 15213 USA. (email: {jlee6, arathod2, kgoel1, jsteckle, wtabib}@andrew.cmu.edu.)

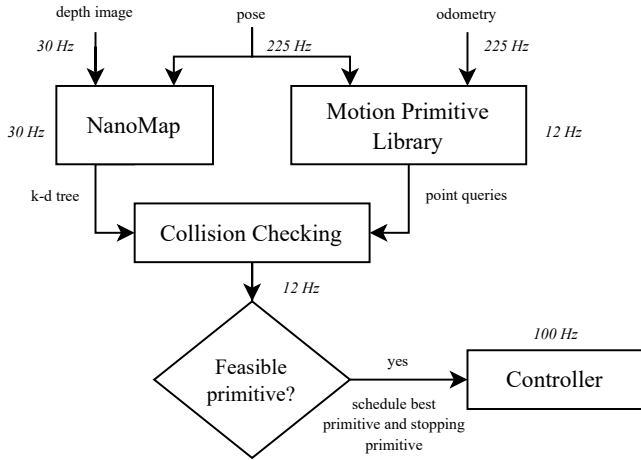


Fig. 2: System diagram of the navigation algorithm. Given depth images and odometry, NanoMap [7] is used for collision avoidance and a library of forward-arc motion primitives is generated for motion planning. To maintain safety, collision-free trajectories are scheduled such that a feasible stopping action is always available within the known free space.

## II. RELATED WORK

This section reviews collision avoidance and planning methods for agile navigation with RGB-D sensors in unknown environments.

Learning-based methods have recently been proposed for rapid flight [1, 2]; however, these methods lack strict collision-free guarantees and may not generalize to environments outside the training domain, which are necessary for deployment in disaster response scenarios. Reactive (memoryless) methods, on the other hand, act directly on instantaneous sensor data or maintain a short spatio-temporal history. RAPPIDS [3] generates trajectories within the latest depth image and iteratively partitions free space into rectangular pyramids for efficient collision detection; however, the planner is prone to becoming trapped in cluttered environments due to the pyramidal corridor constraints and lack of yaw control. BiTE [4] accelerates collision checks with a local occupancy grid by pre-computing a bitwise map and trading off increased memory usage for a fixed path library. This library, however, is not continuous for higher-order derivatives of velocity. NanoMap [5] searches for the minimum uncertainty view of a queried point in space by maintaining a short temporal history of depth images and their relative poses. Ji et al. [6] improves upon NanoMap and constructs a forward spanning tree to find a safe flight corridor for trajectory generation.

Our approach is most similar to Florence et al. [7], which utilizes NanoMap for collision queries. However, their trajectory representation demands high control effort and lacks guaranteed safe stopping behaviors. In contrast, our approach always includes a safe stopping trajectory, ensuring the robot will stop in known free space if no feasible action exists.

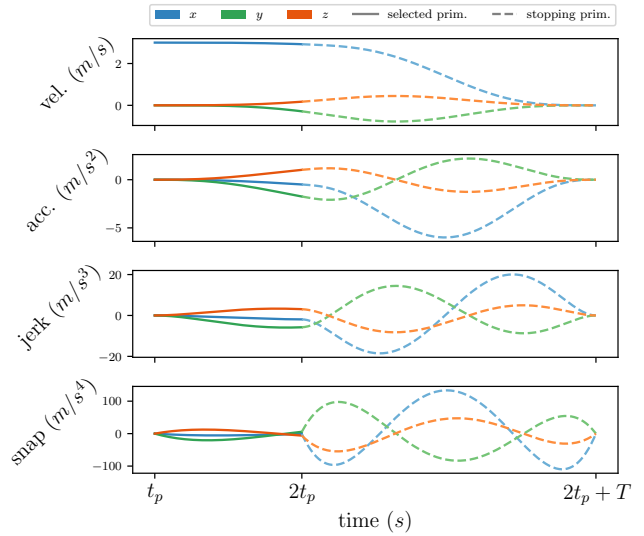


Fig. 3: Derivatives of the scheduled trajectory are continuous up to snap and smooth up to jerk. The planning strategy ensures the robot stops in a safe region.

## III. TECHNICAL APPROACH

This section details the perception and planning strategy for rapid navigation. The high-level system architecture for the approach is illustrated in Fig. 2. A forward-arc motion primitive library is used to generate smooth actions, which are evaluated for collisions. The perception system maintains a 3D point cloud representation of the local environment and searches over a history of observations. Of the feasible motion primitives, the one with the lowest cost is scheduled for execution. Additionally, a safe stopping primitive is scheduled, which is executed if no feasible motion primitive is found at the next planning round.

### A. Forward-Arc Motion Primitive Library

Forward-arc motion primitives propagate the dynamics of a unicycle model for time  $T$  and are parameterized by a desired yaw rate and forward and vertical velocities [8]. This action formulation is differentiable up to jerk and continuous up to snap (see Fig. 3), which is advantageous for aggressive multirotor flight where large angular velocities and accelerations are directly related to the jerk and snap of the reference position [9, 10].

Let  $\mathcal{B}$  represent the body frame of the multirotor. The position and heading of the vehicle is represented as  $\xi_t = [x \ y \ z \ \theta]^\top$ . The linear velocities are expressed in the body frame as  $[v_{x,t}^{\mathcal{B}} \ v_{z,t}^{\mathcal{B}}]$ . The angular velocity,  $\omega_{z,t}^{\mathcal{B}}$  is expressed about the  $z^{\mathcal{B}}$  axis. The equations of the motion primitives are given by the solutions to the unicycle model [10, 11]:

$$\xi_{t+T} = \xi_t + \begin{bmatrix} \frac{v_{x,t}^{\mathcal{B}}}{\omega_{z,t}^{\mathcal{B}}} (\sin(\omega_{z,t}^{\mathcal{B}} T + \theta_t) - \sin(\theta_t)) \\ \frac{v_{z,t}^{\mathcal{B}}}{\omega_{z,t}^{\mathcal{B}}} (\cos(\omega_{z,t}^{\mathcal{B}} T) - \cos(\omega_{z,t}^{\mathcal{B}} T + \theta_t)) \\ v_{z,t}^{\mathcal{B}} T \\ \omega_{z,t}^{\mathcal{B}} T \end{bmatrix}. \quad (1)$$

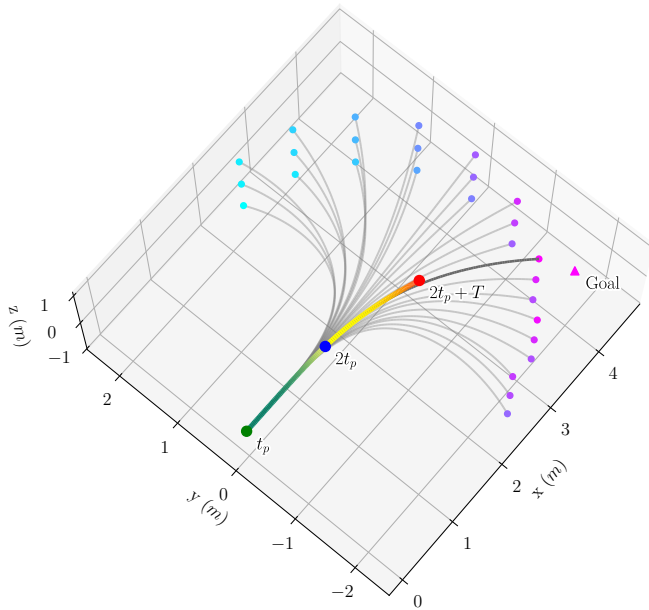


Fig. 4: Illustrative example of trajectory scheduling with the motion primitive library. The motion primitives in the library are shown in gray. The cost of each primitive is evaluated by computing the Euclidean distance between the endpoint and goal (shown as a pink triangle). The endpoints are shown as dots colored from purple to blue, where more pink indicates closer to the goal. Motion primitives that are in collision are pruned. The primitive with lowest cost (shown in dark gray) is selected for execution. The selected primitive segment is scheduled from times  $[t_p, 2t_p]$  and the stopping primitive is scheduled from  $[2t_p, 2t_p + T]$ .

The motion primitive,  $\gamma$ , is parameterized by  $\mathbf{a}_t = \{v_{x,t}^B, v_{z,t}^B, \omega_t^B\}$  and duration  $T$ .  $v_{x,t}^B$  is fixed by the user.  $v_{z,t}^B \in \mathcal{V}_z$  and  $\omega_t^B \in \Omega$  are varied according to a user-specified discretization. The motion primitive library,  $\Gamma$ , is generated as the set of motion primitives created by varying  $v_{z,t}^B$  and  $\omega_t^B$  (see Fig. 4 for an illustration of the library).

Motion primitives are scheduled at a fixed planning rate as shown in Figs. 3 and 4. The selected primitive is executed from  $[t_p, 2t_p]$ . The stopping primitive is scheduled from  $[2t_p, 2t_p + T]$  so that if the next planning round fails to find a feasible motion primitive, the robot stops in free space.

### B. Local 3D Perception and Collision Checking

Nanomap [5] is used for high-rate proximity queries for collision avoidance. We provide a brief overview of the query search algorithm, which uses  $k$ -nearest neighbor queries over a short temporal history of depth measurements.

NanoMap maintains a chain of edge-vertex pairs where each edge contains the relative transform  $T_{S_{i-1}}^{S_i}$  between consecutive sensor frames and each vertex contains the ordered point cloud and corresponding  $k$ -d tree. The motion primitive representing the position of the vehicle,  $\gamma^{(0)}$ , is sampled in time using a fixed  $\Delta t$  up to the trajectory duration,  $T$ , to generate query points,  $\mathbf{p}_{\text{query}}^B \in \mathbb{R}^3$ .

$$\mathbf{p}_{\text{query}}^B = \gamma^{(0)}(t). \quad (2)$$

Query points sampled from the motion plan are iteratively transformed into previous sensor frames until a view containing the query point is found. The transformation to the

$i$ -th coordinate frame is obtained by

$$\mathbf{p}_{\text{query}}^{S_i} = \prod_{j=1}^i \left[ T_{S_{j-1}}^{S_j} \right] T_{S_0}^{S_i} \mathbf{p}_{\text{query}}^B \quad (3)$$

Once a query is determined to be in view, the ordered point cloud is used to determine whether the point is within free space, after which the  $k$ -d tree is used to evaluate the  $k$ -nearest neighbors. Note that in Eq. (3), the uncertainty propagation of the query point is disabled. This modification is made because we leverage a more accurate optimization-based visual inertial navigation system (detailed in following sections) for state estimation compared to what is used in [7].

For each query position,  $\mathbf{p}_{\text{query}}^B$ , the distance,  $d$ , is found between  $\mathbf{p}_{\text{query}}^B$  and the nearest neighbor in the depth image. For a user-specified collision radius  $r_{\text{coll}}$ , the primitive is marked infeasible if  $d < r_{\text{coll}}$ . Feasible primitives are scored using the Euclidean distance to the goal position,  $g$ , from the end of the primitive,  $\text{Cost}(\gamma, g) = \|g - \gamma^{(0)}(T)\|_2$ . The primitive that minimizes the cost function is scheduled. Figure 2 shows an overview of the final algorithm along with operating frequencies.



Fig. 5: (a)–(c) illustrate a subset of the simulation environments used to validate the proposed approach.

## IV. RESULTS

The approach is evaluated in simulation (see Sections IV-A and IV-B) and with hardware experiments (see Section IV-C). In simulation evaluations, the proposed approach is compared against two reactive vision-based methods, RAPPIDS [3]<sup>1</sup> and Florence et al. [7]<sup>2</sup>, which demonstrate local planning in unknown environments. For the rest of this section, we will refer to these approaches as *RAPPIDS* and *Florence*, respectively, and to the proposed approach as *Forward-Arc*. We disable the “dolphin” oscillations of [7], which were used to improve state estimation, because this is perfectly known in simulation. Primitives that modulate z-height were found to cause crashes due to altitude drift, so these were also removed. To set the desired speed for *RAPPIDS* we adjust the allocated trajectory duration such that the planner achieves this speed in an open field. We also use a velocity tracking yaw angle to enable navigation in unstructured environments and generalize beyond the corridor environments tested in [3].

<sup>1</sup><https://github.com/nlbucki/RAPPIDS>

<sup>2</sup>[https://github.com/peteflorence/nanomap\\_ros](https://github.com/peteflorence/nanomap_ros)

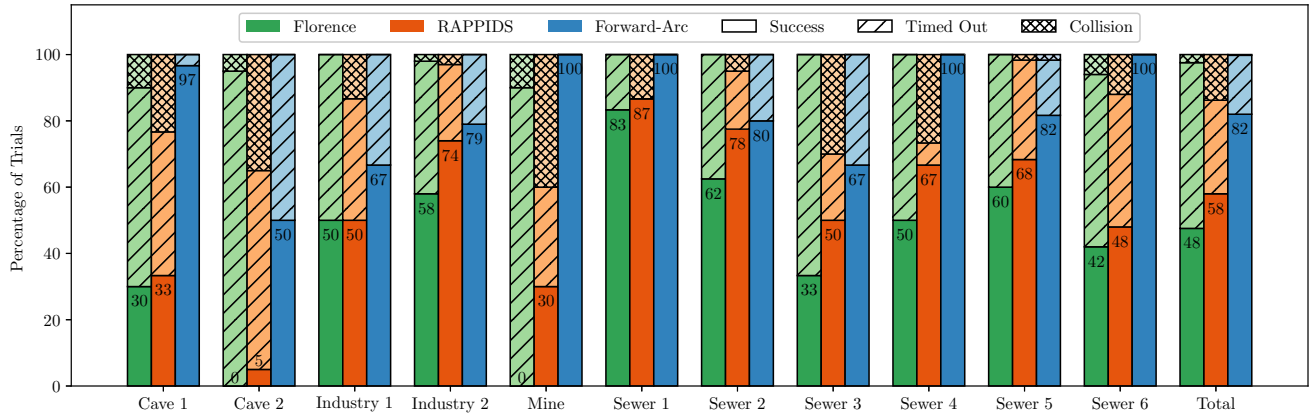


Fig. 6: Planner success rate and failure modes across the environments detailed in Table I. The proposed method (*Forward-Arc*) achieves the highest success rate and lowest collision rate compared to the baseline reactive planners [3, 7]. A total of 1350 trials are run (450 for each approach).

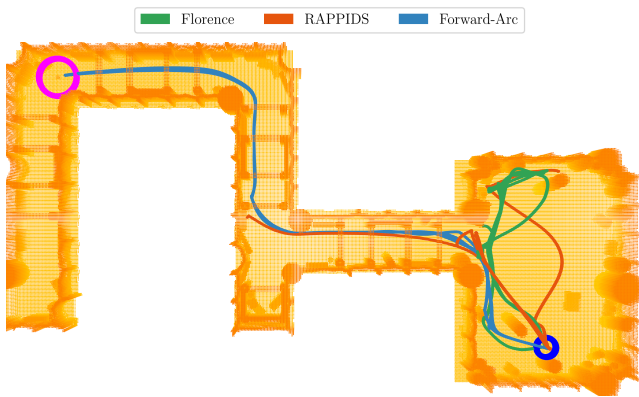


Fig. 7: Cross-section of the mine environment with overlays of 5 trajectories for each planning approach. The start and goal locations are indicated in blue and magenta, respectively. *Forward-Arc* reaches the goal in all 5 trials. *RAPPIDS* collides in 4 trials and times out in 1 trial. *Florence* collides in 1 trial and times out in 4 trials.

Two simulation evaluations are conducted. First, diverse environments representative of disaster scenarios are used to evaluate the success rate of reaching a goal within a specified time (detailed in Section IV-A). Second, simulations that vary the obstacle density (e.g. forest-like environments) are detailed in Section IV-B. In addition to the success rates, this second set of simulation experiments evaluates the approaches in terms of flight time, path length, and control effort. The Flightmare simulator [12] is used to generate photorealistic images and depth maps at 30 Hz. Simulations are run on a desktop computer with the planner running on a single thread of an Intel i9-14900K CPU. An NVIDIA RTX 4090 GPU is leveraged for photorealistic rendering within Flightmare.

#### A. Simulated Disaster Scenarios

Simulations are conducted in caves, a mine, abandoned industrial environments, and a sewer system (Fig. 5). Multiple start and goal locations are specified to evaluate the robustness of each approach. For each pair of start and goal locations each planner is run 5 times for a total of 1350 trials

TABLE I: Unity Custom Environments

Scene	# Goals	Trials	Description
Cave 1	6	90	Natural, Corridors
Cave 2	8	120	Natural, Caverns
Industry 1	6	90	Man-made, Buildings
Industry 2	20	300	Man-made, Factory
Mine	2	30	Man-made, Corridor
Sewer 1	6	90	Man-made, Rooms
Sewer 2	8	120	Man-made, Rooms
Sewer 3	6	90	Man-made, Rooms
Sewer 4	6	90	Man-made, Tunnels
Sewer 5	12	180	Man-made, Rooms
Sewer 6	10	150	Man-made, Tunnels

(see Table I). A trial is considered successful if the robot reaches the goal within a time limit. The sensing range is set to 10 m for all planning approaches.

The planner performance is evaluated by measuring the success rate and failure modes (collisions and timeouts). The results are reported in Fig. 6. *Forward-Arc* outperforms the baseline methods in terms of success rate (82%) and has the fewest collisions (1 out of 450 trials). In contrast, we find that many *Florence* collisions are caused by aggressive emergency stopping maneuvers, which results in a loss of stability. Figure 7 provides a representative figure for the performance of each of the approaches. *RAPPIDS* is unable to make sharp turns due to narrow pyramidal flight corridor constraints. *Florence* is unable to enter the passageway due to its conservative collision probability and uncertainty propagation estimates. *Forward-Arc* consistently navigates to the objective, demonstrating robust and safe operation in diverse environmental conditions.

#### B. Obstacle Density Experiments

Next, we study the effect of varying obstacle densities and desired speeds on planner performance. We design a forest-like environment using Poisson disk sampling with a uniform density and cylindrical obstacles with a diameter of 0.75 m. Start and goal locations are positioned 70 meters apart with 10 evenly spaced endpoints per random environment seed

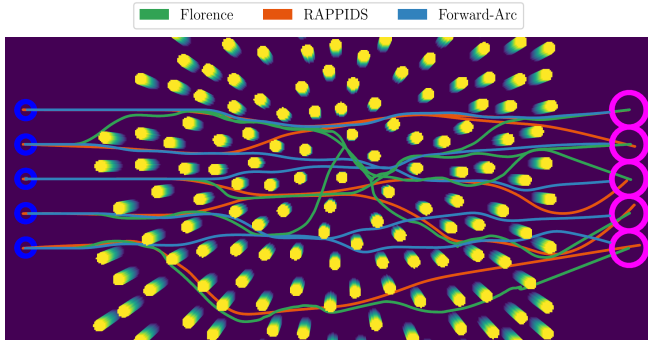


Fig. 8: Overlay of 5 trajectories for each planner on the ground truth point cloud ( $v_{max} = 3m/s$  and  $\rho = 0.075$  obstacles/ $m^2$ ). *Forward-Arc* takes the shortest path towards the goal compared to the baselines.

(see Fig. 8 for example). We run a total of 1800 trials with 50 trials per planner at each combination in desired speed and obstacle density.

In Fig. 9a, *Florence* struggles with high density environments due to its aggressive stopping maneuvers and conservative collision probability propagation. *RAPPIDS* has an increased flight time at high obstacle densities due to the lack of explicit yaw angle control leading it to take longer paths (Fig. 8). As shown in Figs. 9a and 9b, *Forward-Arc* exhibits the lowest collision rate, flight time, path length, and control effort (integral of jerk squared) and has the highest success rate amongst all variations in obstacle densities and speeds.

### C. Hardware Experiments

A custom quadrotor platform is developed for evaluation in hardware experiments. It is equipped with a forward-facing Intel RealSense D455 (Fig. 10), a downward-facing LW20 range finder, and a Matrix Vision BlueFox global shutter greyscale camera. The monocular visual inertial navigation system of Yao [13] is used for GPS-denied state estimation.

The system is fully autonomous and all calculations are conducted onboard a NVIDIA Orin AGX equipped with 32 GB of RAM. The total system mass is 2.8 kg. The RealSense generate depth images at 30 Hz with a resolution of  $424 \times 240$ . The re-planning algorithm runs at 12 Hz, and maintain a 1 s history of frames. We utilize a cascaded controller (the outer loop runs at 100 Hz), which runs on the NVIDIA Orin. An mRo Pixracer flight controller runs the attitude control loop at a higher frequency with modified PX4 firmware.

Experiments are conducted in three environments: (1) an outdoor flight arena, (2) forest, and (3) cave.



Fig. 10: The aerial robot used in hardware experiments is equipped with a D455 and NVIDIA Orin AGX.

1) *Outdoor Drone Arena*: 11 high speed flight experiments were conducted in an outdoor space with an area of  $18m \times 24m$ . Foam boards with dimension 2m high by 1m wide are used as obstacles. The flight statistics for the 11 flight experiments are shown in Fig. 11 and Table II. The goal location for all trials was set to be 18m from the starting point, while desired speed and obstacle locations varied over the trials. The maximum speed achieved was 6 m/s. All 11 trials were successful (over 205m total path length).

2) *Forest*: The approach was tested under the canopy of a stand of trees over 9 trials. Start and goal positions varied with a goal distance of 15m up to 80m. The maximum forward velocity was set to 5 m/s. A trial is visualized in Fig. 12

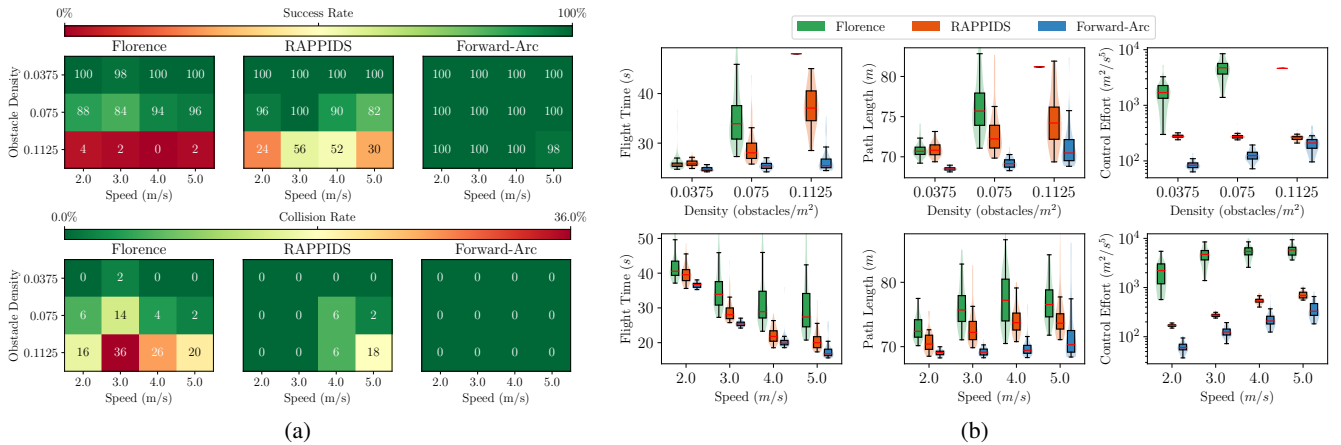


Fig. 9: (a) success rate and collision rate matrices for simulations that vary obstacle densities and speeds. The *Forward-Arc* approach has higher rates of success at higher obstacle densities and speeds compared to the baseline approaches. (b) distribution of planning performance metrics from successful simulation trials across varying obstacle densities and speeds. Note that a log scale is used for the control effort plots. *Forward-Arc* reaches the objective with lower average flight time, path length, and control effort metrics compared to the baseline approaches.

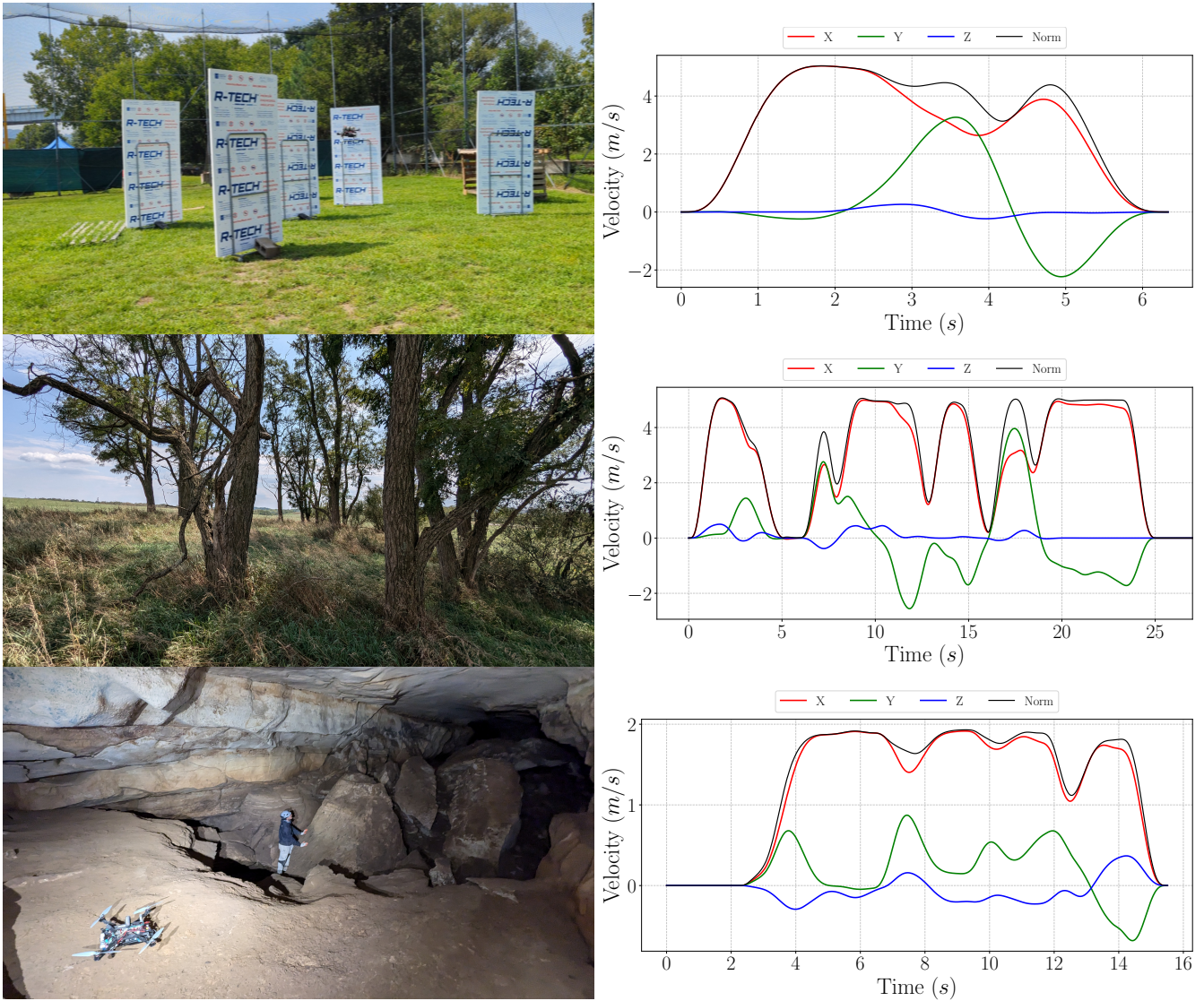


Fig. 11: Left: flight arena, forest, and cave test environments. Right: reference trajectory velocity profiles for flights 10, 7 and 4, respectively, from Table II. The maximum achieved speed across all trials is 6 m/s.

3) *Cave*: The final set of experiments deployed the robot to a cave in Kentucky. The cave features large rock outcrops and a deep chasm. The goal position varied between 10 m and 20 m away. Over 6 trials, four trials succeeded, one timed out, and one ended in collision. The cave features narrow sections with a vertical gap less than 1.8 m. The desired forward velocity was set between 2 m/s and 3.5 m/s.

#### D. Discussion on failure modes

As shown in Table II we experienced three failure modes in hardware experiments. First, perception errors due to thin branches that were not detected by the depth sensor led to 3 collisions in the forest environment. Second, without a global planner, the robot got stuck in a dead end in the cave environment where navigation to the goal required backtracking. Lastly, cave flight 6 experienced a collision due to VINS state estimation drift. During execution of a stopping maneuver, particulates from rotor downwash caused incorrect

feature matches in the downward-facing camera, which led to the robot tracking the stopping trajectory into the ground instead of at the correct altitude.

#### V. CONCLUSION

In this work we propose a reactive navigation method using a history of depth images and forward-arc motion primitives. We evaluate the performance of *Forward-Arc* against two baseline reactive methods in diverse simulation environments. *Forward-Arc* achieves the highest success rate and lowest collision rate in all environments, demonstrating the efficacy of the primitive scheduling approach and safe stopping strategy. Additionally, *Forward-Arc* reaches the objective in obstacle density experiments with lower average flight time, path length, and control effort metrics compared to the baselines. Finally, we conduct hardware trials in a flight arena, forest, and cave environments to validate the approach in diverse, real-world conditions. A maximum

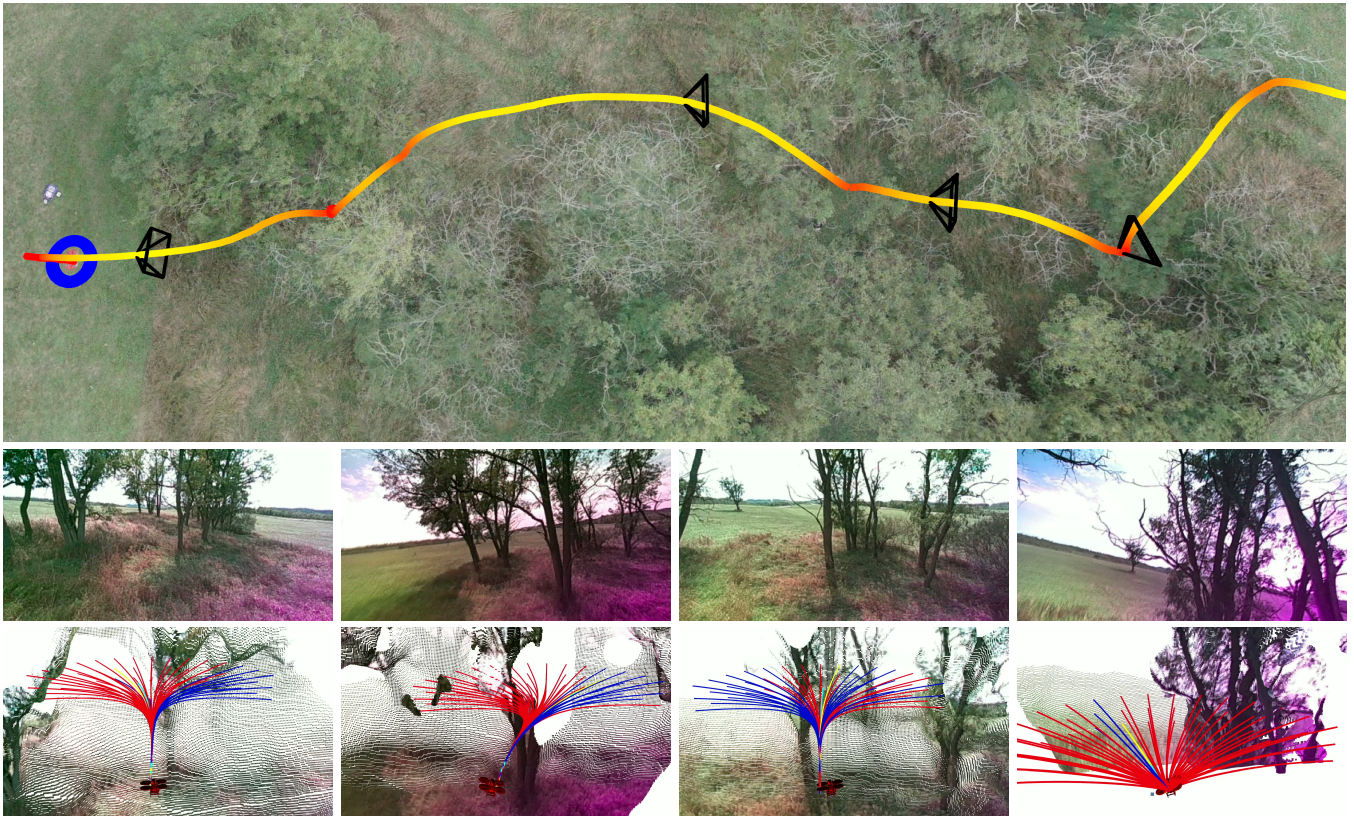


Fig. 12: Outdoor obstacle avoidance test under tree canopy (forest flight 7 in Fig. 11 and Table II). Top: VINS trajectory overlaid on terrain map (low speeds are shown in red and high speeds in yellow). Camera frustums are visualized at four time steps where the robot maneuvers to avoid obstacles. Middle: Onboard RGB image from RealSense D455. Bottom: Robot and forward-arc motion primitive library (red: non-safe primitives, blue: safe primitives, yellow: selected primitive, cyan: stopping primitive).

TABLE II: Hardware Flight Trials

Env.	Flight #	Flight Time <i>s</i>	Path Length <i>m</i>	$v_{max}$ <i>m/s</i>	Max Speed <i>m/s</i>	Avg Speed <i>m/s</i>
Outdoor Flight Arena	1	12.08	16.45	2	2.21	1.32
	2	9.62	17.48	3	3.04	1.76
	3	7.01	17.89	4	4.09	2.29
	4	10.71	17.69	3	3.04	1.52
	5	9.40	18.71	4	4.12	1.83
	6	8.12	17.58	4	4.01	2.06
	7	6.94	17.85	5	4.85	2.46
	8	7.65	19.85	5	5.11	2.43
	9	9.22	20.49	5	5.09	2.11
	10	8.36	22.14	5	5.02	2.54
	11	7.13	18.23	6	6.06	2.38
Forest	1	9.73	19.88	3	3.11	1.90
	2	9.68	14.77	3	3.50	1.42
	3♣	11.57	29.91	3	3.30	2.53
	4	9.15	30.36	5	5.13	3.10
	5	18.43	64.20	5	5.20	4.34
	6♣	4.77	15.86	5	5.07	3.25
	7	33.62	91.28	5	5.22	2.58
	8	22.23	87.79	5	5.29	3.81
	9♣	36.40	29.47	5	5.05	0.71
Cave	1	7.79	10.30	2	1.91	1.23
	2	13.98	14.23	2	2.08	0.86
	3	11.05	12.98	2	2.05	1.11
	4	13.96	20.97	2	2.34	1.39
	5♦	11.69	13.45	3	3.43	1.06
	6♣	6.05	12.04	3	3.16	1.87

♣ indicates a crash due to thin obstacle not being detected.

♦ indicates robot did not find a safe route and timed out.

♣ indicates robot crashed due to VINS state estimate drift.

speed of 6 m/s is achieved over 571 m without collisions in successful trials. Potential avenues for future work include adapting the desired forward velocity to varying levels of environment clutter and incorporating a hierarchical global planner to enable the robot to escape dead ends.

## VI. ACKNOWLEDGMENT

The authors would like to thank E. Burkholder for field testing support. The authors would also like to thank K. Bailey and T. Miller for facilitating experiments at the cave in Kentucky.

## REFERENCES

- [1] A. Loquercio, E. Kaufmann, R. Ranftl, M. Müller, V. Koltun, and D. Scaramuzza, “Learning high-speed flight in the wild,” *Science Robotics*, vol. 6, no. 59, p. eabg5810, 2021.
- [2] Y. Zhang, Y. Hu, Y. Song, D. Zou, and W. Lin. Back to Newton’s Laws: Learning Vision-based Agile Flight via Differentiable Physics. [Online]. Available: <http://arxiv.org/abs/2407.10648>
- [3] N. Bucki, J. Lee, and M. W. Mueller, “Rectangular pyramid partitioning using integrated depth sensors (rappids): A fast planner for multicopter navigation,” *IEEE Robotics and Automation Letters*, vol. 5, no. 3, pp. 4626–4633, 2020.
- [4] V. K. Viswanathan, E. Dexheimer, G. Li, G. Loianno, M. Kaess, and S. Scherer, “Efficient Trajectory Library Filtering for Quadrotor Flight in Unknown Environments,” in *2020 IEEE/RSJ International Conference on Intelligent Robots and Systems (IROS)*, 2020, pp. 2510–2517.
- [5] P. R. Florence, J. Carter, J. Ware, and R. Tedrake, “Nanomap: Fast, uncertainty-aware proximity queries with lazy search over local

- 3d data,” in *2018 IEEE International Conference on Robotics and Automation (ICRA)*. IEEE, 2018, pp. 7631–7638.
- [6] J. Ji, Z. Wang, Y. Wang, C. Xu, and F. Gao, “Mapless-Planner: A Robust and Fast Planning Framework for Aggressive Autonomous Flight without Map Fusion,” in *2021 IEEE International Conference on Robotics and Automation (ICRA)*. IEEE, 2021, pp. 6315–6321.
- [7] P. Florence, J. Carter, and R. Tedrake, “Integrated perception and control at high speed: Evaluating collision avoidance maneuvers without maps,” in *Algorithmic Foundations of Robotics XII: Proceedings of the Twelfth Workshop on the Algorithmic Foundations of Robotics*. Springer, 2020, pp. 304–319.
- [8] X. Yang, K. Sreenath, and N. Michael, “A framework for efficient teleoperation via online adaptation,” in *2017 IEEE International Conference on Robotics and Automation (ICRA)*. IEEE, 2017, pp. 5948–5953.
- [9] A. Spitzer, X. Yang, J. Yao, A. Dhawale, K. Goel, M. Dabhi, M. Collins, C. Boirum, and N. Michael, “Fast and agile vision-based flight with teleoperation and collision avoidance on a multirotor,” in *Proceedings of the 2018 International Symposium on Experimental Robotics*. Springer, 2020, pp. 524–535.
- [10] X. Yang, A. Agrawal, K. Sreenath, and N. Michael, “Online adaptive teleoperation via motion primitives for mobile robots,” *Autonomous Robots*, vol. 43, pp. 1357–1373, 2019.
- [11] W. Tabib, K. Goel, J. Yao, C. Boirum, and N. Michael, “Autonomous cave surveying with an aerial robot,” *IEEE Transactions on Robotics*, vol. 38, no. 2, pp. 1016–1032, 2021.
- [12] Y. Song, S. Naji, E. Kaufmann, A. Loquercio, and D. Scaramuzza, “Flightmare: A flexible quadrotor simulator,” in *Conference on Robot Learning*. PMLR, 2021, pp. 1147–1157.
- [13] J. W. Yao, “Resource-constrained state estimation with multi-modal sensing,” Ph.D. dissertation, Carnegie Mellon University, Pittsburgh, PA, April 2020.